Paper

Numerical Prediction of Channel-Type Segregation Formation in DC Casting of Al–Mg Billet*

Takuya Yamamoto**, Keisuke Kamiya***, Shohei Yomogida***, Takashi Kubo****, Masanori Tsunekawa***, Keita Fukawa***** and Sergey V. Komarov******

Although channel-type macro-segregations are a well-known defect formed in Direct Chill (DC) casting of aluminum alloys, their formation mechanism remains unclear up to now. To investigate the possible mechanisms, we carried out numerical simulation considering thermo-solutal flow and solidification coupled with phase diagram. The main emphasis is placed on the effect of shrinkage flow and slurry flow on the macro-segregation characteristics. The shrinkage flow causes negative segregations to form along the center axis of billet especially at high casting speeds, while channel-type segregations are not formed under these conditions. On the other hand, the slurry flow in mushy zone results in formation of the channel-type segregations in large billets at low casting speeds. In addition, formation of three types of channel-type segregations is predicted in the following locations (1) flow separation zone, (2) flow stagnant zone, (3) mushy zone where the upward solutal buoyant flow is generated. The formation condition of channel-type segregation is considered using solutal Rayleigh number for binary alloys.

Keywords: *DC casting; Segregation; Numerical analysis;*

1. Introduction

Wrought aluminum alloys are mainly produced by Direct Chill (DC) casting, which is a semi-continuous casting process. In the DC casting process, molten metal is first poured onto a receiving platform called bottom block, which is moved downward at a constant speed. The aluminum melt is gradually solidified inside a mold due to primary cooling and then in water due to secondary cooling, that makes it possible to produce a billet or ingot of several meters in length. The DC casting process has been widely used because of its high productivity. There are, however, many problems to be solved in order to fabricate ingots with uniform structure without cracks and other defects. That is why a lot of efforts have been put to understand the formation mechanism of defects occurring in the DC casting process. Previous studies, dealt with these issues, were reviewed by Emley and Nadella et al[1), 2)]. For instance, such defects as the deformation of ingot at its bottom part called Butt curl, cracking formation due to hot tearing, formation of wavy structure on the ingot surface, non-uniform distribution of alloy elements over the ingot called macro-segregation have been well known for a long time. In the present study, we focused on the macro-segregations.

Macro-segregations during DC casting have been documented experimentally in many studies. For example, Eskin et al. investigated a radial distribution of copper composition using a pilot-scale DC caster and an Al-4.5mass% Cu alloy[3)]. The macro-segregation characteristics was found to vary with the flow rate of cooling water and casting speed. The effect of melt temperature and casting speed on the macro-segregation pattern has also been systematically investigated[4)]. In addition, the effect of grain refiners on the macro-segregation characteristics during DC casting has been evaluated for a variety of alloys[5)]. However, many factors affect the macro-segregation

* The main part of this paper has been published in Metallurgical and Materials Transaction B **52** (2021), 4046-4060.

** Department of Chemical Engineering, Osaka Metropolitan University, Associate Professor, Ph.D. (Eng.)
*** Research Department Ⅱ, Research & Development Center, Marketing & Technology Division, UACJ Corporation
**** Research Department Ⅱ, Research & Development Center, Marketing & Technology Division, UACJ Corporation, Ph. D. (Eng.)
***** Casting Technology Department, Nagoya Works, Flat Rolled Products Division, UACJ Corporation
****** New Industry Creation Hatchery Center, Tohoku University, Project Professor, Ph.D. (Eng.)

formation during DC casting, and experimental investigation of some of them faces great difficulties because of the absence of appropriate measurement and observation tools, especially at high temperature conditions.

To understand underlying mechanisms and suppress the macro-segregation formation during DC casting, a variety of numerical models have been developed in the last 25 years. The first numerical model describing macro-segregations was developed by Bennon and Incropera[6]. Then, this model was improved by Ni and Beckermann[7], and extended to the DC casting simulation by Reddy and Beckermann[8]. Later, Thevik et al. performed a numerical analysis aiming at surface segregations[9], Vreeman et al. proposed a numerical model considering free-floating dendrites[10], and Vreeman and Incropera investigated the effect of free-floating dendrites on the macro-segregation pattern in Al-Cu and Al-Mg alloy systems[11]. It was reported that the macro-segregation pattern is dependent on the solid fraction at which free-floating dendrites forms rigid and solid structure. This value is called "packing solid fraction". Later, Vreeman et al. carried out numerical simulation concerning industrial scale billets, and found that the results are in good agreement with their experimental results[12]. Then, Zaloznik et al. predicted macro-segregations in Al-4.5mass% Cu and Al-5.25mass % Cu billets[13)~15)] and in 7449 ingots[16]. However, the above-mentioned numerical models of macro-segregations are unstable and spatially non-bounded. Therefore, the effect of discretization scheme in numerical simulation on concentration distribution was also investigated by Venneker and Katgerman[17]. Eskin et al. proposed a scaling law for macro-segregations by numerical results[18]. Early studies on macro-segregations in DC casting up to the 2000s have been reviewed by Nadella et al.

In the 2010s, macro-segregations in the DC casting process have been also the object of numerical investigations. Combeau and Zaloznik's group developed a numerical model of macro-segregation behavior coupled with the microstructural behavior[19], This numerical model was used later on to evaluate the effect of alloy composition on macro-segregation characteristics in ingots[20]. Besides, a simplified three-phase multiscale model was proposed[21], and validated[22]. Finally, based on this model, three-dimensional phenomena were predicted[23]. In addition, Krane's research group has elucidated the behavior of unsteady macro-segregations pattern in 7050 alloy billets taking into account the bottom block movement[24]. Then, the authors evaluated the effect of wiper application on macro-segregation pattern[25]. The wiper application is known to be one of the usable methods allowing one to prevent cooling water from flowing down along the ingot surfaces. In addition, they investigated the dependence of macro-segregation pattern on the liquid metal feeding[26]. In addition, Lebon et al. investigated the macro-segregation behavior during ultrasonic DC casting[27] and melt-conditioned DC casting[28].

Although many phenomena have been elucidated and numerically simulated as mentioned above, the mechanisms of channel-type macro segregation formation in the DC casting process remain poorly

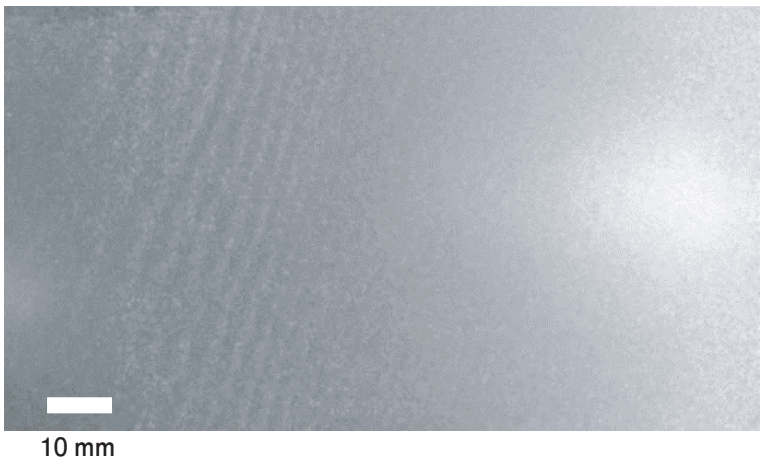

Fig. 1 A sample photograph of channel-type macro-segregations formed in an ingot manufactured by DC casting.

understood. Particularly, although the formation condition has been clarified in the directional solidification and mold casting[30)~32)], little is known about formation of channel-type macro-segregations in DC casting process, which were experimentally observed by Li et al[29)]. A sample photograph of channel-type macro-segregations formed in an ingot manufactured by DC casting is shown in **Fig. 1**. It is to be noted that this type of macro-segregations is a problem of great concern in DC casting because such segregations can form concentration stripes in aluminum products as shown in Fig. 1. To shed light on the formation condition of channel-type macro-segregation in a DC casting process, we carried out numerical simulation focusing on two kinds of flow. The first one is a shrinkage flow, which is caused by volume shrinkage due to solidification. The second one is a slurry flow, which is generated in the zone of free-floating dendrites. It was found that the slurry flow causes formation of channel-type macro-segregations of three types depending on the formation location. The formation conditions of these macro segregations were clarified in terms of Rayleigh number.

2. Simulation Model

A schematic diagram of the computational domain is shown in **Fig. 2**. In this numerical simulation, we focused on the phenomena occurring during the hot-top DC casting. The aluminum melt, supplied from the hot-top unit, is first cooled in the mold, and then solidified further in the water-cooling section. We investigated the formation of channel-type macro-segregations in an 5052 alloy billet. However, in the present simulation, Al-2.5mass% Mg alloy was used to simplify the numerical model. In this study, calculations were performed in the axisymmetric approximation. In addition, the following assumptions were made to model the thermo-solutal flow with solidification during the casting process.

- The thermodynamic relationships are determined by phase diagram.
- Aluminum melt is an incompressible fluid, and buoyancy flow is modeled using the Boussinesq approximation.
- Physical properties are independent of temperature. Fluid resistance in the mushy region is governed by the Blake-Kozeny law.
- Dimension of ingot remains unchanged after solidification.
- The packing effect due to rigid dendrite structure is determined only by the volume fraction of solid.
- Based on these assumptions, the following numerical model was developed.

Based on these assumptions, the following numerical model was developed.

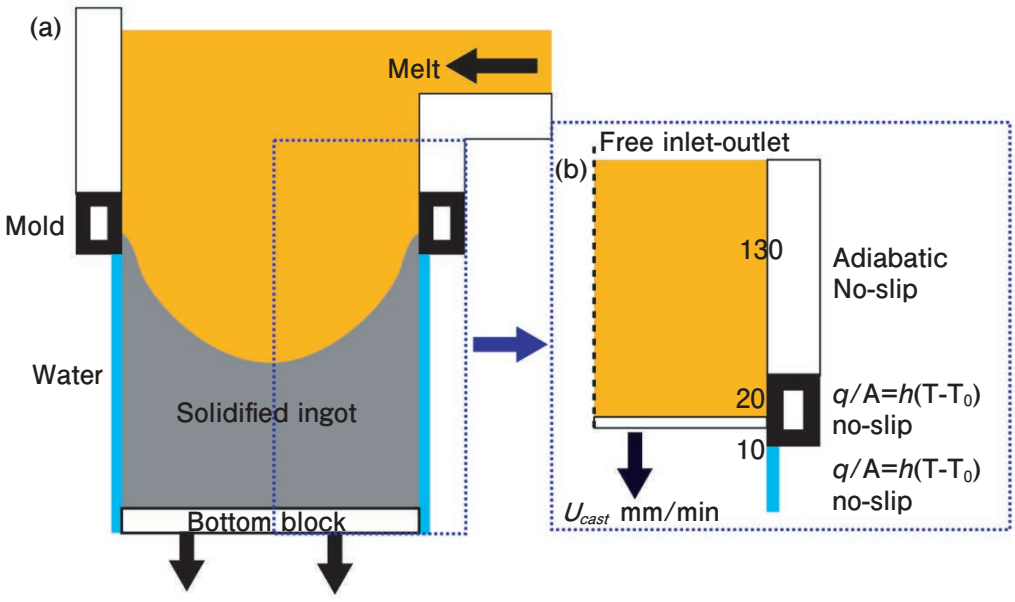

Fig. 2 Schematic representation of calculation domain: (a) melt sump and solidified ingot, and (b) simplified calculation domain with boundary conditions.

2.1 Governing equations

We basically followed the numerical modeling proposed by Vreeman et al[10]. and modified by Fezi et al[24]. The basic governing equations for the momentum, mass, enthalpy and species concentration balance with solidification are given as

$$\frac{\partial(\rho \boldsymbol{u})}{\partial t} + \nabla(\rho \boldsymbol{u}\boldsymbol{u}) = -\nabla p + \nabla\cdot\left(\frac{\mu_l}{\rho_l}\nabla \boldsymbol{u}\right) + \rho \boldsymbol{B} + \boldsymbol{S} \quad (1)$$

$$\frac{\partial \rho}{\partial t} + \nabla\cdot(\rho \boldsymbol{u}) = 0 \quad (2)$$

$$\frac{\partial(\rho h)}{\partial t} + \nabla\cdot(\rho \boldsymbol{u} h) = \nabla\cdot\left(\frac{k}{c_{ps}}\nabla h\right) + \nabla\cdot\left(\frac{k}{c_{ps}}\nabla(h_S - h)\right) - \nabla\cdot\left(\rho(\boldsymbol{u} - \boldsymbol{u}_S)(h_l - h)\right) \quad (3)$$

$$\frac{\partial(\rho C)}{\partial t} + \nabla\cdot(\rho \boldsymbol{u} C) = \nabla\cdot(\alpha_l \rho_l D_l \nabla C) + \nabla\cdot(\alpha_l \rho_l D_l \nabla(C_l - C)) - \nabla\cdot\left(\rho(\boldsymbol{u} - \boldsymbol{u}_S)(C_l - C)\right) \quad (4)$$

where ρ is the density, $\boldsymbol{u}$ is the mixture flow velocity, t is the time, p is the pressure, μ is the viscosity, $\boldsymbol{B}$ is the buoyancy force, $\boldsymbol{S}$ is the source term for mushy and solid zones, h is the enthalpy, k is the thermal conductivity, c_p is the heat capacity of solid, C is the composition, α is the volume fraction, D is the diffusion coefficient. The subscripts s and l indicate the solid and liquid phases, respectively.

The buoyancy force and mushy terms can be written as

$$\boldsymbol{B} = -\boldsymbol{g}\beta_T(T - T_0) - \boldsymbol{g}\beta_C(C - C_0) \quad (5)$$

$$S = (1 - P)S_{Slurry} + PS_{rigid} \quad (6)$$

where $\boldsymbol{g}$ is s the gravitational acceleration, β_T is the volume thermal expansion coefficient, β_C is the volume solutal expansion coefficient, T_0 is the reference temperature, C_0 is the reference composition, P is the packing variable, proposed by Plotkowski and Krane[32], Coleman and Krane[26] as

$$P = min\left(max\left(\left(1 - \frac{\alpha_S^C - \alpha_S}{\Delta\alpha_S}\right), 0\right), 1\right) \quad (7)$$

Where α_S^C is the critical volume fraction of solid phase, and $\Delta\alpha_S$ is the steepness of phase transition. The packing variable, P, is changed depending on the mass fraction of solid, and the slurry and mushy zones are determined by the smooth function. The mushy and rigid source terms are described as

$$S_{Slurry} = -\nabla\cdot\left(\mu_l \frac{\rho f_S}{\rho_l}\nabla \boldsymbol{u}_S\right) + \nabla\cdot\left(\overline{\mu_S}(1 - \alpha)\nabla \boldsymbol{u}_S\right) = -\nabla\cdot\left[\left(\frac{\rho f_S}{\rho_l}\right)(\boldsymbol{u} - \boldsymbol{u}_S)(\boldsymbol{u} - \boldsymbol{u}_S)\right] \quad (8)$$

$$S_{rigid} = -\frac{\mu_l}{K}\frac{\rho}{\rho_l}(\boldsymbol{u} - \boldsymbol{u}_S) \quad (9)$$

where $\overline{\mu_S}$ is the effective solid viscosity as used by Vreeman *et al.*,[10] f is the mass fraction, and K is the permeability, which is described by the following Blake-Kozeny model

$$K = \frac{\lambda^2}{180}\frac{\alpha_l^3}{(1 - \alpha_l)^2} \quad (10)$$

where λ is the secondary dendrite arm spacing. The solid velocity $\boldsymbol{u}_S$ is modeled as

$$\boldsymbol{u}_S = (1 - P)\left(\boldsymbol{u} + f_l\left(\frac{\alpha(\rho_S - \rho_l)d_g^2}{18\mu_l}\boldsymbol{g}\right)\right) + P\boldsymbol{u}_{cast} \quad (11)$$

where $\boldsymbol{d_g}$ is the diameter of floating solid particle, and u_{cast} is the casting velocity. The volume fraction α was modeled on the basis of error function formulation, which was proposed by *y* Rosler and Bruggemann[33].

$$\alpha = \frac{1}{2}erf\left(\frac{4(T - T_m)}{T_l - T_S}\right) + \frac{1}{2} \quad (12)$$

2.2 Thermodynamic relationships

We followed the numerical modelling for the thermodynamic relationships proposed by Prakash and Voller[34], as has been implemented in our previous study[35]. **Fig. 3** is a representation of linearized phase diagram used in the present simulation. Using such a phase diagram, the mass fraction of liquid can be calculated as

$$f_l = 1 - \frac{1}{1 - k_p}\frac{T - T_{liq}}{T - T_m} \quad (13)$$

where k_p is the partition coefficient, T_m is the melting temperature of pure aluminum, and T_{liq} is the liquidus temperature, which is described as

$$T_{liq} = T_m + \left(T_e - T_m\right)\frac{C}{C_e} \tag{14}$$

where T_e is the eutectic temperature, and C_e is the eutectic concentration.

To avoid numerical oscillations due to calculation error, we adopted the same algorithm as that proposed by Prakash and Voller[34]. First, one can obtain the following relationship by arranging Eq.[13]. as

$$T = F\left(f_l, C\right) = \frac{T_{liq} - \left(1-f_l\right)\left(1-k_P\right)T_m}{1-\left(1-f_l\right)\left(1-k_P\right)} \tag{15}$$

A dependence of enthalpy on the liquid fraction can be given as

$$h = c_P T + f_l L \tag{16}$$

where L is the latent heat. After updating the enthalpy at the nth iteration, this expression becomes

$$h^{n+1} = c_P T^n + f_l^n L \tag{17}$$

By substituting Eq. [15] into Eq. [17], one can obtain the following relationship

$$c_P F\left(f_l^{n+1}, C^n\right) + f_l^{n+1} L = c_P T^n + f_l^n L \tag{18}$$

By substituting Eq. [15] into Eq. [18], the following quadratic equation can be obtained.

$$a\left(f_l^{n+1}\right)^2 + b\left(f_l^{n+1}\right) + d = 0 \tag{19}$$

where a, b, d are the coefficients, which have been formulated and explained in details in our previous study.[35] The mass fraction f_l can be calculated by solving Eq. [19] as

$$f_l^{n+1} = min\left(\max\left(0, \frac{-b+\sqrt{b^2-4ad}}{2a}\right), 1\right) \tag{20}$$

By solving the governing equations coupled with the above-mentioned calculation of thermodynamic relationship, stable convergence can be achieved. The liquidus and solidus concentration are updated as

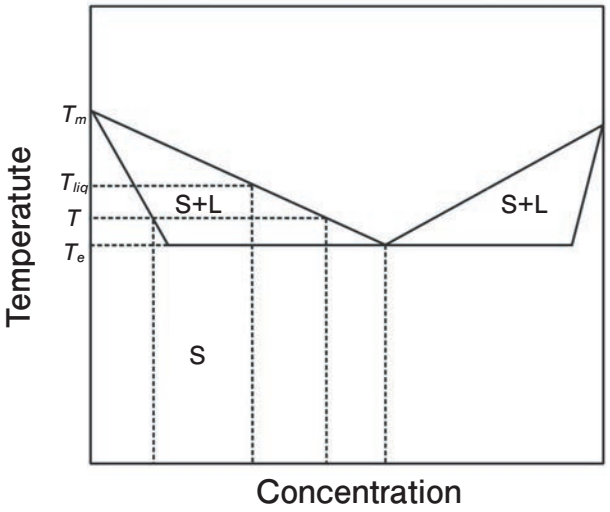

Fig. 3 A representation of linearized phase diagram.

$$C_l^{n+1} = \frac{C^n}{1+\left(1-f_l^{n+1}\right)\left(k_P-1\right)} \tag{21}$$

$$C_S^{n+1} = \frac{k_P C^n}{1+\left(1-f_l^{n+1}\right)\left(k_P-1\right)} \tag{22}$$

During the iterations, the physical properties are also updated as

$$\rho^{n+1} = \alpha_l \rho_l + \alpha_S \rho_S \tag{23}$$

$$k^{n+1} = f_l k_l + f_S k_S \tag{24}$$

$$c_p^{n+1} = f_l c_{Pl} + f_S c_{pS} \tag{25}$$

2.3 Boundary conditions and numerical grid

The boundary conditions are shown in Fig. 2. The boundary conditions are similar to those in our previous study[36]. At the top boundary, the free inlet and outlet conditions were imposed, at which the flow velocity and direction are determined by the pressure gradient normal to the boundary. Here, the inlet temperature and concentration were set to 950 K and 2.5mass% , respectively. At the adiabatic side wall, no-slip condition was imposed for flow velocity, and normal fluxes of heat and species to the boundary were set to zero. At the water-cooled boundary, a slip condition was used for flow velocity, and normal gradient of pressure and concentration to the boundary was set to zero. The boundary condition for temperature at the water-cooled boundary was governed by the Newton's cooling law, and the heat

transfer coefficient was set to be as a function of cooled water flow rate, Q and temperature, T, as proposed by Weckman and Niessen[37].

$$h = \left(-1.67\times10^{5}+704T\right)Q^{\frac{1}{3}}+\frac{20.8\left(T-373.15\right)^{3}}{T-273.15} \quad (26)$$

The water flow rate was set to be 110 L/min in the present study. According to Eq.[26], at higher temperatures, the heat transfer coefficient becomes unrealistically large. Therefore, the Eq.[26] was used in a temperature range below 423 K. Above this temperature, the heat transfer coefficient was set to 10,000 W/(m^2K). At the bottom block and mold surface, the heat transfer coefficient was set to 2000 and 3000 W/(m^2K), respectively.

In DC casting, typical length of billets produced is several meters, and therefore in the simulation the size and aspect ratio of calculation domain are changed in wide ranges. Hence, the numerical grid must be rearranged as the calculations proceed. In the present study, the dynamic grid motion was implemented by adding new grid cells from the moving boundary as used in our previous study[36, 38]. This dynamic grid motion enables one to simulate the phenomena occurring during DC casting with higher accuracy and higher grid resolution. The length of grid cell in each direction was set to 0.5 mm.

2.4 Other calculation models

The parameters used in the present study are shown in **Table 1**. The physical properties are based on the relevant literature data[39, 40]. The physical properties of melt and solid corresponded to those at 950 K and 723 K. The temperature dependence of physical properties was neglected in the present study because the variation of physical properties due to the phase change is much larger than that due to temperature variation in the present temperature range.

The convective terms in governing equations were discretized by the limited linear scheme, which is one of the Total Variation Diminishing (TVD) schemes. The other spatial derivatives were discretized by the linear interpolation scheme. The time advancement was modeled by the second order backward scheme. The coupling between pressure and velocity fields was modeled by pressure implicit with splitting operator (PISO) algorithm[41]. All the above numerical models were incorporated into an open-source software, OpenFOAM (v1812)

3. Result and Discussion

3.1 Validation of calculation program

First, to validate our simulation model, we

Table 1 Parameters used in the present study.

Variable		Value	Unit
Melt Density (950 K)	ρ_l	2.45×10^{3}	kg m^{-3}
Heat Capacity of Melt (950 K)	c_{pl}	1.13×10^{3}	J kg^{-1} K^{-1}
Kinematic Viscosity	ν	5.43×10^{-7}	m^2 s^{-1}
Thermal Conductivity of Melt (950 K)	k_l	6.91×10^{1}	W m^{-1} K^{-1}
Diffusion Coefficient (950 K)	D	1.14×10^{-8}	m^2 s^{-1}
Thermal Expansion Coefficient	β_T	6.9×10^{-5}	K^{-1}
Solutal Expansion Coefficient	s_C	4.8×10^{-1}	—
Solid Density	ρ_s	2.56×10^{3}	kg m^{-3}
Heat Capacity of Solid	c_{ps}	1.07×10^{3}	J kg^{-1} K^{-1}
Solid Thermal Conductivity	k_s	1.38×10^{2}	W m^{-1} K^{-1}
Eutectic Temperature	T_e	7.23×10^{2}	K
Melting Temperature of Pure Aluminum	T_m	9.34×10^{2}	K
Partition Coefficient	k_p	0.47	—
Eutectic Concentration (Mass Fraction)	C_e	0.38	—
Latent Heat	L	3.77×10^{5}	J kg^{-1}
Gravitational Acceleration	g	9.81×10^{0}	m^1 s^{-2}
Critical Solid Volume Fraction	α_{sc}	0, 0.3	—
Smooth Parameter of Packing Fraction	$\Delta\alpha_s$	0.05	—
Secondary Dendrite Arm Spacing	λ	5.00×10^{-5}	m
Diameter of Floating Particle	d_p	7.50×10^{-5}	m
Averaged Solid Viscosity	$\overline{\mu}_s$	6.45×10^{-3}	Pa s
Billet Radius	R	0.05, 0.101, 0.2	m
Casting Speed	u_{cast}	50, 100, 200	mm/min

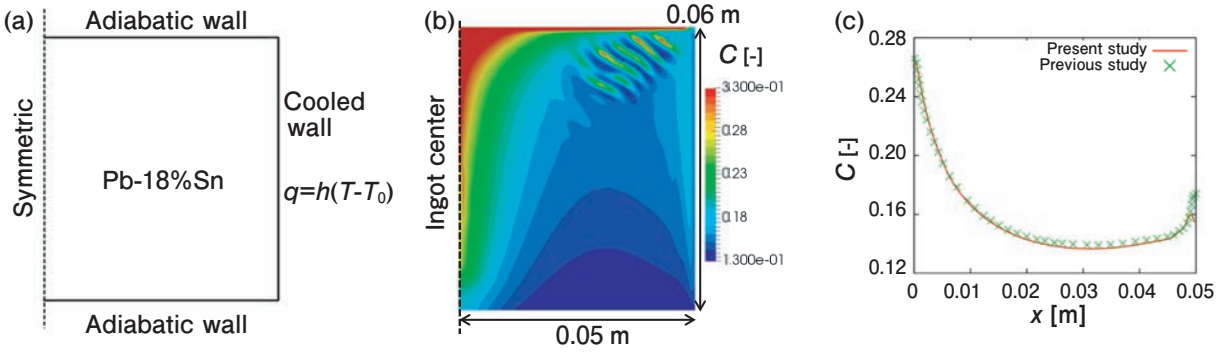

Fig. 4 Validation results of simulation code: (a) numerical domain, (b) distribution of Sn mass fraction at the end of solidification, and (c)distribution of Sn mass fraction along the horizontal line (Color figure online).

compared the numerical results with those of previous studies[31), 42)]. In these studies, solidification phenomena of Pb-18mass% Sn alloy in a rectangular domain were investigated. It is to be noted that this alloy system has been widely used for the validation and verification of simulation codes on macro-segregation characteristics. The numerical domain is shown in **Fig. 4**(a). The domain was filled with the Pb-18mass%Sn alloy melt at a temperature of 558 K. The heat was released from the side wall according to the Newton's cooling law. The heat transfer coefficient, h and ambient temperature, T_0 used in the Newton's cooling relationship were set to be 400 $Wm^{-2}K^{-1}$ and 298 K, respectively. The other calculation conditions are the same as those in the above-mentioned validation case[31), 42)].

The calculated distribution of Sn mass fraction at the end of solidification is shown in Fig. 4(b). This distribution is similar to that of the previous study[31)]. Near the upper right corner, a striped pattern of higher Sn concentrations is formed. Such a pattern is called channel-type segregation. In the case of hypoeutectic alloy, the Sn concentration becomes higher in the interdendritic liquid during solidification according to phase diagram. The liquid with high Sn concentration forms a counterclockwise circulating flow, which transports the Sn-enriched liquid upward along the solidification front. This causes a solidification delay resulting in formation of liquid channels there. To compare the present simulation results with previous ones quantitatively, the concentration distribution along a horizontal line located at a distance of 10 mm from the bottom boundary, is shown in Fig. 4(c). It is seen that the

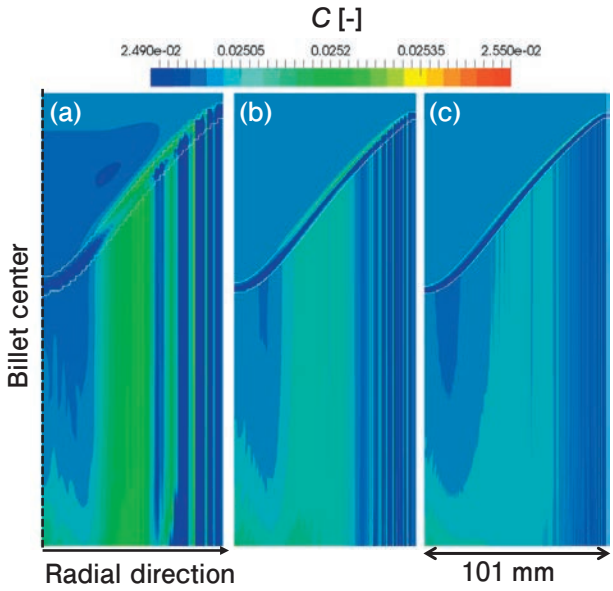

Fig. 5 Distribution of Mg concentration in the sump and solidified part of ingot with shrinkage flow at a casting speed of 100 mm/min at t = 200 s. with different grid resolutions: (a) coarse, (b) normal and (c) fine resolutions (Color figure online).

distributions are in a good agreement to each other. Therefore, this confirms that the calculation code developed in the present study is capable of predicting the macro-segregation phenomena including the channel-type segregation accurately.

3.2 Influence of solidification-driven shrinkage flow on Mg concentration

First, in order to evaluate the accuracy of numerical predictions the effect of numerical grid resolution on the calculation results was clarified for the case with shrinkage flow. **Fig. 5** shows the distribution of Mg concentration over a billet of 101 mm in radius at a casting speed of 100 mm/min with shrinkage flow. The simulated time in this figure is 200 seconds. In the figure, white lines indicate

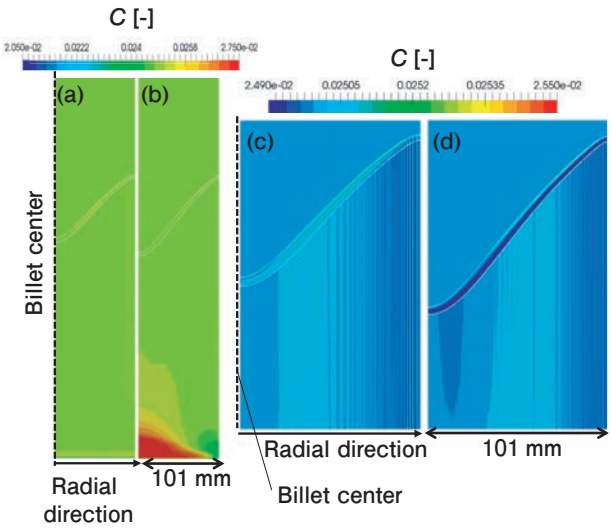

Fig. 6 Effect of shrinkage flow on the distribution of Mg concentration at a casting speed of 100 mm/min (a, c) without and (b, d) with shrinkage flow. (c, d) are magnified figures near the mushy zone (Color figure online).

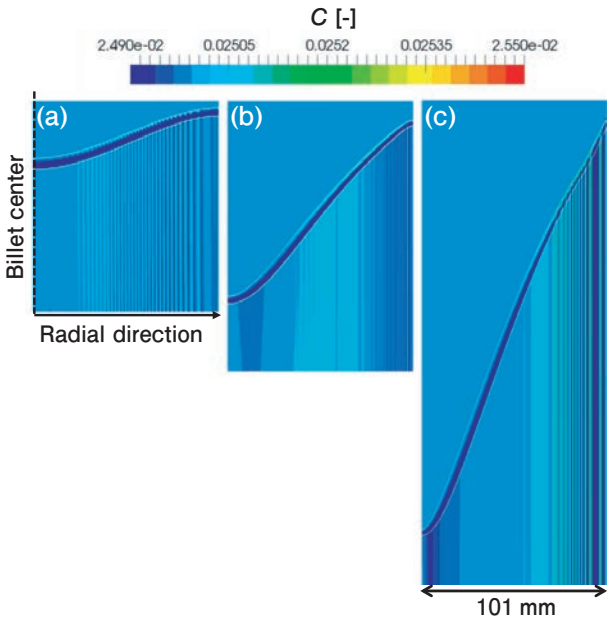

Fig. 7 Distribution of Mg in the sump and ingot with shrinkage flow at a casting speed of (a) 50 mm/min, (b) 100 mm/min, and (c) 200 mm/min (Color figure online).

locations of the solidus and liquidus temperatures. In the present calculation, three grid resolutions, namely coarse, normal and fine, with sizes of 2, 1, and 0.5 mm were evaluated. Although the concentration distribution and the sump shape are almost the same in all three numerical grid resolutions, the spatial oscillations of composition are larger in the cases of coarse and normal grid resolutions. These results indicate that the numerical grid influence is small, and, therefore, the calculation accuracy is sufficiently high in the case of fine grid resolution. Therefore, we used the fine grid in the following simulation.

Next, the effect of shrinkage flow on the distribution of Mg will be considered. **Fig. 6** shows the Mg concentration distribution predicted at a casting speed of 100 mm/min with and without shrinkage flow. In the case with shrinkage flow, three characteristic features can be distinguished: (1) Mg concentration becomes larger near the bottom block, (2) Mg concentration is small in the mushy zone, and (3) negative segregation pattern occurs at the billet centerline. The shrinking direction is normal to the solidification front. Therefore, the negative segregation pattern occurs near the center-line of billet. The phenomena (2) and (3) were already reported previously in several studies[11), 13)～18), 24), 26)].

Next, the effect of casting speed on the macro-segregation characteristics was investigated for the case with shrinkage flow. **Fig. 7** shows the distribution of Mg concentration near the sump predicted under different casting speeds. The sump depth becomes larger with increase of casting speed. In addition, the negative segregation pattern, observed near the central axis, becomes larger with increase of casting speed. The increase in the sump depth at higher casting speeds causes the horizontal velocity of shrinkage flow to increase that results in a significant formation of negative macro-segregations along the centerline.

As discussed above, the shrinkage flow during solidification causes the negative segregations to occur near the center axis of billet. The negative segregations are pronounced at high casting speed. However, no the channel-type macro-segregations pattern was observed in all these cases.

3.3 Influence of slurry flow on macro-segregations

First, the effect of numerical grid resolution on the distribution of Mg concentration was evaluated using a slurry flow model. **Fig. 8** shows the Mg distribution predicted under different numerical grid resolutions at a casting speed of 100 mm/min in a billet of 101 mm in radius. Three white lines indicate the locations of solidus and liquidus temperatures, and packing location corresponding to the zone where a rigid dendrite structure starts to be formed. It is seen

that the spatial oscillations in Mg concentration due to numerical error decreases as the grid resolution becomes finer. Therefore, the fine grid resolution was used in the following simulation.

Next, the effect of slurry flow on the distribution of Mg concentration was investigated. **Fig. 9** shows the results predicted for a casting speed of 100 mm/min predicted with and without the slurry flow model at t = 200 seconds. When the slurry flow model is used, the simulation predicts melt flows in the mushy zone between the packing and liquidus lines, and the flow forms an eddy at the center location between the center axis and billet surface. This eddy causes Mg to be localized in the mushy zone, resulting in formation of the channel-type Mg segregations.

Subsequently, the effect of casting speed on the macro-segregation characteristics was further investigated. **Fig. 10** shows the time variation in Mg concentration distribution predicted with slurry flow model at different casting speeds. The billet radius was the same, 101 mm. At an early stage of casting, Mg is segregated in the mushy zone due to the partition between solid and liquid phases as shown in Fig. 10(a,i), (b,i) and (c,i). The Mg-enriched zone is then floated up near the center axis of billet due to a solutal buoyancy flow as seen from Fig. 10(a,ii), (b,ii) and (c,ii). Finally, the flow, temperature and concentration fields are stabilized reaching pseudosteady states as shown in Fig. 10(a,iii), (b,iii) and (c,iii). It is seen that the Mg distribution is strongly dependent on the casting speed. At slow casting speeds (Fig. 10(a) and (b)), the buoyancy flow results in formation of a high concentration zone in the mushy zone between the billet wall and center axis, which is a cause of the channel-type segregations in the solidified ingots. On the other hand, no the high concentration zone and channel-type segregations pattern were observed in the simulation at the 200 mm/min casting speed (Fig. 10(c)). This difference can be explained by an influence of downward flow, which is generated due to motion of solidified ingot. The flow velocity vectors near the mushy zone are shown in **Fig. 11**. With increase of casting speed, the velocity of downward flow becomes larger, and this flow is opposite to the

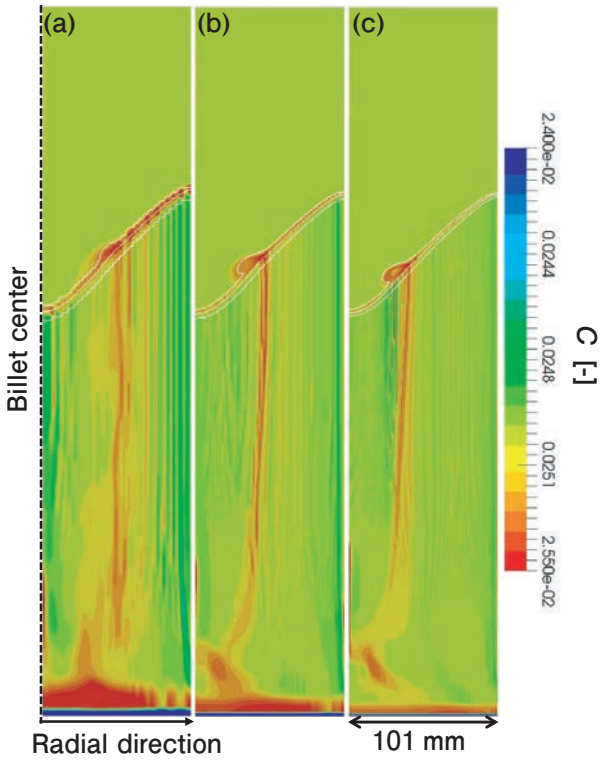

Fig. 8 Effect of numerical grid resolution on the distribution of Mg concentration over a billet of 101 mm in radius when the slurry flow model was used at a casting speed of 100 mm/min: (a) coarse, (b) normal and (c) fine grid resolutions. The simulated time is 200 s (Color figure online).

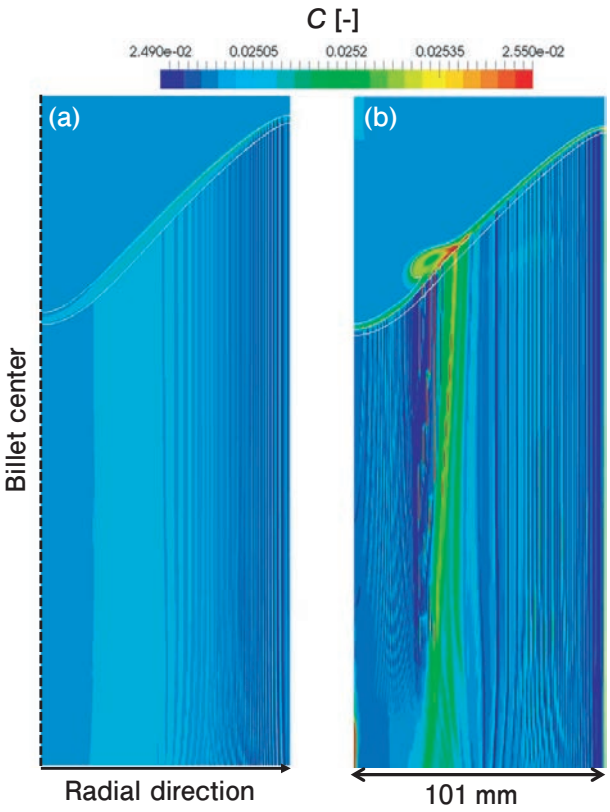

Fig. 9 Effect of slurry flow on the distribution of Mg concentration at a casting speed of 100 mm/min: (a) without and (b) with slurry flow model. The billet radius is 101 mm (Color figure online).

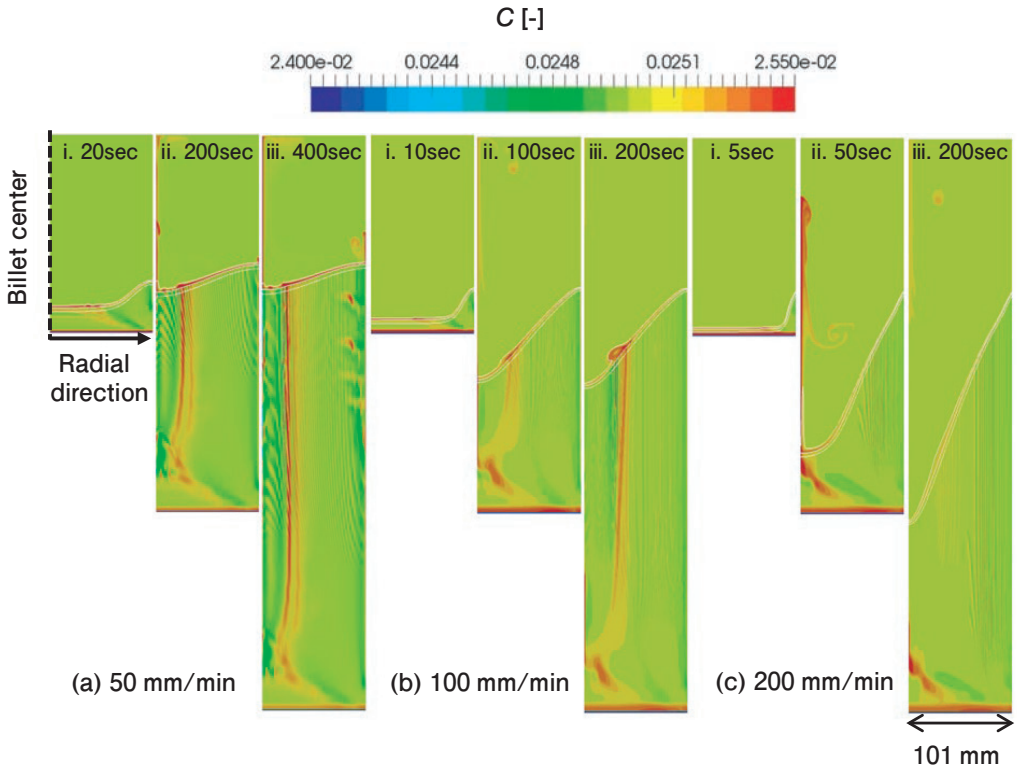

Fig. 10 Time variation in Mg distribution predicted with slurry flow model at different casting speeds: (a) 50 mm/min, (b) 100 mm/min, and (c) 200 mm/min. The billet radius is 101 mm. The simulated time is (i) 20, (ii) 200, and (iii) 400 s in case (a); (i) 10, (ii) 100, and (iii) 200 s in case(b); (i) 5, (ii) 50, and (iii) 100 s in case (c) (Color figure online).

solutal buoyancy flow. Therefore, the larger downward flow at higher casting speed overcomes the buoyancy flow. Finally, the effect of billet radius on the macro-segregation characteristics was evaluated. **Fig. 12** shows the effect of billet size on the distribution of Mg at a casting speed of 100 mm/min. In the case of smaller radius, 50 mm, no buoyancy flow is developed as shown in Fig. 12(a). As the billet radius increases, the velocity of solutal buoyancy flow becomes larger. In addition, in the billet of largest radius examined, the fluctuating non-linear convection is developed. This continuously oscillating vortical flow causes formation of the striped-pattern channel-type segregations. Time variation of Mg concentration distribution over a billet of 200 mm in radius is shown in **Fig. 13**. The casting speed was set to be 100 and 200 mm/min. In both the cases, the striped-pattern channel-type segregations were found to be formed. Until the sump shape is stabilized as shown in Fig. 13(a) i-iii and (b) i-v, the solutal buoyancy flow is under development at the center axis of billet. After development and stabilization of the sump shape, a complicated vortical flow is formed in the sump as shown in Fig. 13(a) iv-vii and (b) vi-vii. This flow leads to formation of thin zones enriched with Mg in the mushy zone. This causes a delay in the solidification and formation of the striped-pattern channel-type segregations. Also, as shown in Fig. 13, negative segregations are formed between the high-concentration channels. To elucidate the possible formation mechanisms of these channel-type segregations, the interaction between the flow and concentration fields was investigated in more details. These channel-type segregations can be subdivided into the following three types depending on location where they are formed: an upward flow developed along the solidification front, the flow separation zone and stagnant zone. **Fig. 14** shows the time variation in Mg concentration and flow velocity vectors near the mushy zone at a casting speed of 100 mm/min in a billet with 200 mm radius at the location where the upward buoyant flow is developed. A zone with high concentration of Mg is created at the packing location (α_{SC}) because of enrichment of the liquid phase with Mg due to its partition between the solid and liquid phases. The concentration of Mg in the mushy zone causes occurrence of the upward solutal buoyancy flow that leads to the accumulation of Mg along the

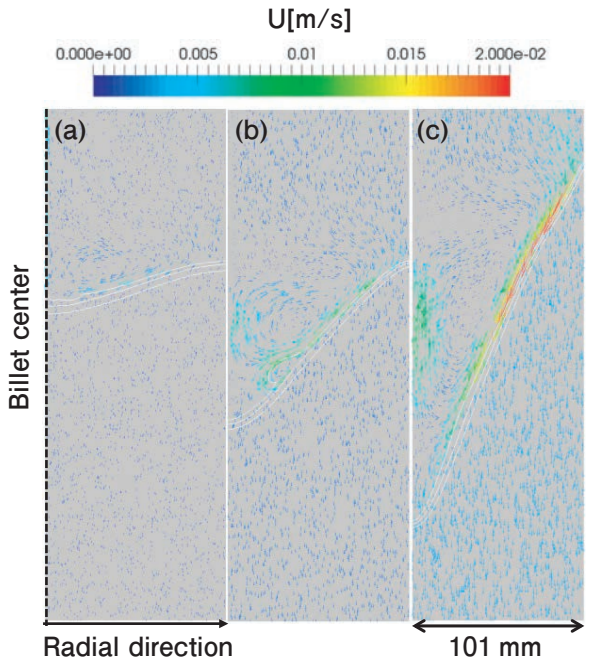

Fig. 11 Velocity distribution near the mushy zone at the casting speed of (a) 50 mm/min, (b) 100 mm/min, and (c) 200 mm/min after the stabilization of sump shape. The white lines indicate the solidus temperature, liquidus temperature and packing location (Color figure online).

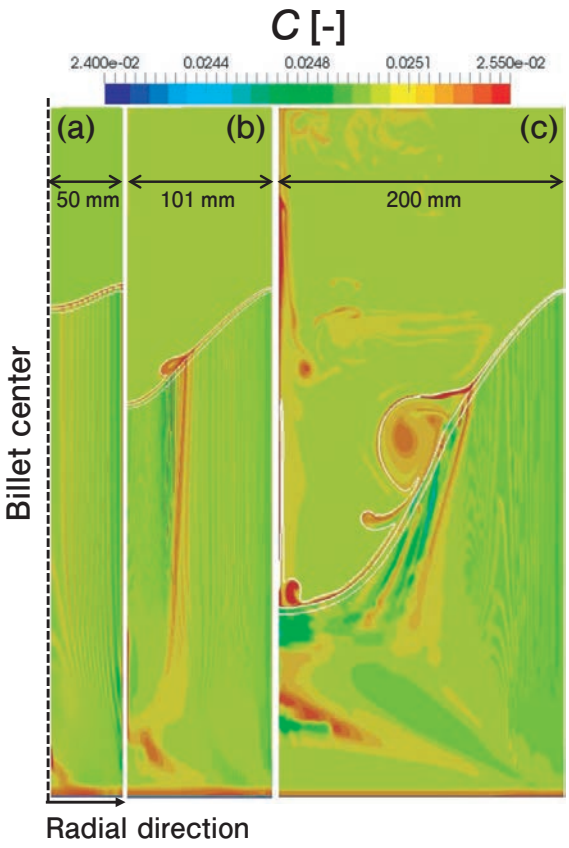

Fig. 12 Effect of billet size on the Mg concentration distribution at a casting speed of 100 mm/min. The radius of billet is (a) 50 mm, (b) 101 mm, and (c) 200 mm (Color figure online).

packing locations resulting in the solidification delay. As a result, Mg is transferred from the low concentration zone toward the high concentration zone of delayed solidification due to Mg partition between the solid and liquid phase. In this way, the low concentration zones (negative segregations) are formed below the high concentration zones at the packing location. **Fig. 15** shows the interaction between the slurry flow and vertically aligned channel-type negative segregations for the case of large billet of 200 mm in radius and casting speed of 100 mm/min in the flow separation zones indicated in Fig. 15 by red circles. These zones are created by the buoyancy flow. As a result, the locations of high Mg concentration are shifted, and zones of lower Mg concentration are produced in the mushy zone underneath the flow separation zones forming the channel-type negative segregations aligned in the vertical direction. The generation mechanism of these channel-type segregations is different from that of the striped-pattern channel-type segregations at the upward flow as discussed above. **Fig. 16** shows the interaction between the slurry flow and vertically aligned channel-type segregations in the stagnant zone in a billet with the radius of 200 mm at the casting speed of 100 mm/min. The stagnant zones are indicated by black circles. It is seen that these zones are located close to the flow separation zone, and zones of high Mg concentration are formed there. As a result, the vertical channel-type segregations are created.

The velocity of buoyant flow can be expressed in terms of Rayleigh number. As explained above, the solutal buoyant flow causes formation of the channel-type segregations. The thermal and solutal buoyancy flow can be evaluated by the following Rayleigh number.

$$Ra_T = \frac{g\beta_T \Delta T R^3}{\nu\alpha} \tag{27}$$

$$Ra_S = \frac{g\beta_C \Delta C R^3}{\nu D} \tag{28}$$

where the ΔT is the temperature difference, and ΔC is the concentration difference. The temperature and composition differences can be roughly calculated

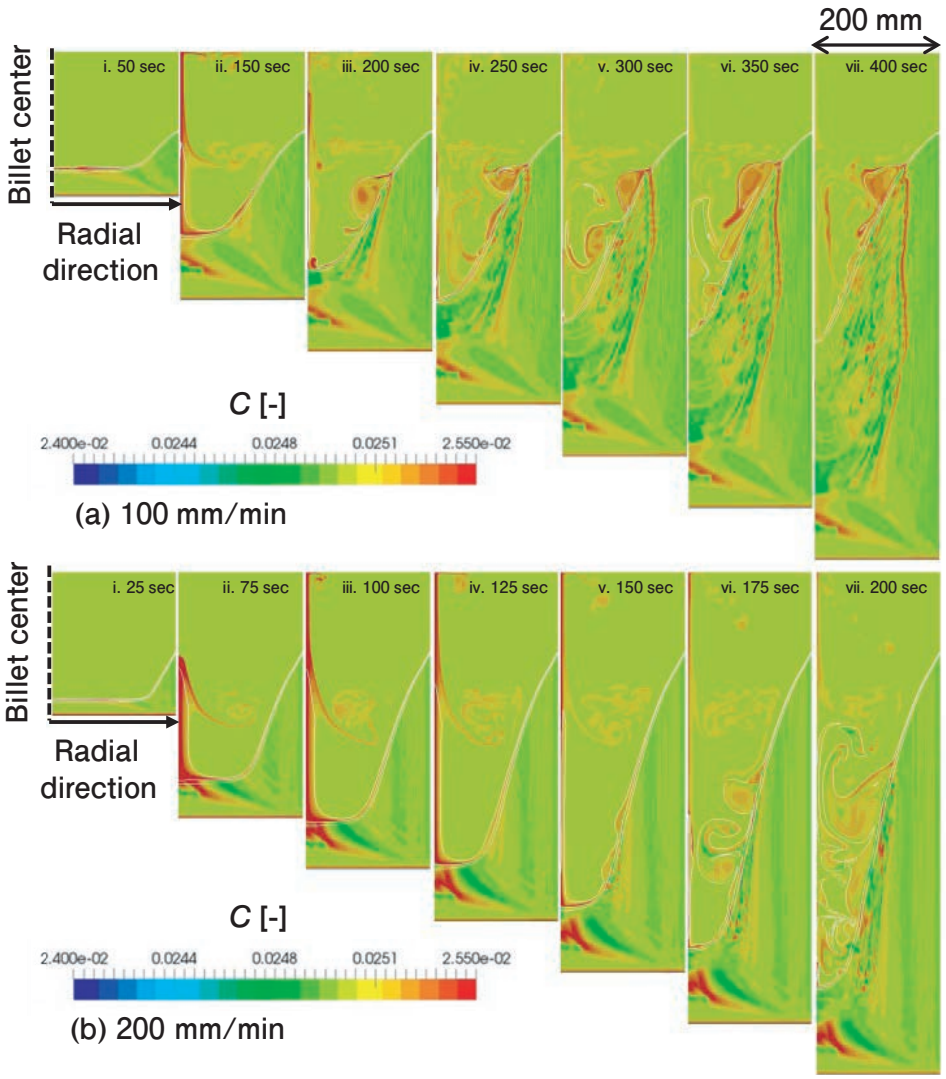

Fig. 13 Time variation of Mg concentration distribution over a billet of 200 mm in radius at the casting speed of (a) 100 mm/min and (b) 200 mm/min. The simulated time is (i) 50, (ii) 150, (iii) 200, (iv) 250, (v) 300, (vi) 350, and (vii) 400 s in case (a); (i) 25, (ii) 75, (iii) 100, (iv) 125, (v) 150, (vi) 175, and (vii) 200 s in case (b) (Color figure online).

as

$$\Delta T = T_{cast} - T_{l,C_{cast}} \tag{29}$$

$$\Delta C = C_{l,C_{cast}} - C_{cast} = C_{cast}\left(\frac{1}{1+\alpha_S C\left(k_P - 1\right)}\right) - C_{cast} \tag{30}$$

The thermal and solutal Rayleigh numbers are approximately 7.691×10^5 and 3.700×10^9. These values indicate that the solutal buoyancy flow is much stronger than thermal buoyancy flow. This suggests that the solutal buoyancy flow is the main cause of the channel segregation formation. Also, the solutal Rayleigh number is proportional to the first power of concentration difference and third power of billet radius. It means that the condition for formation of channel-type segregations is sensitive to the billet size. Therefore, as seen in Fig. 12 through 16, the channel-type segregations are formed easily in large billets. Finally, one important point should be explained concerning the difference in the formation conditions of channel-type segregations between mold and DC castings. In the directional and mold casting, the channel-type segregations are formed at low cooling rates[43]. However, in DC casting, despite the fact that cooling rates are even lower than those in a mold casting, the channel-type segregations are formed only in some special cases. Besides, in mold and directional castings, the channel-type segregations can be simulated without considering the slurry flow model[30)~32)]. The simulated results without using the slurry flow model in mold and directional casting also indicate the formation of channel-type segregations is expected to be more difficult in a DC casting compared with in a mold

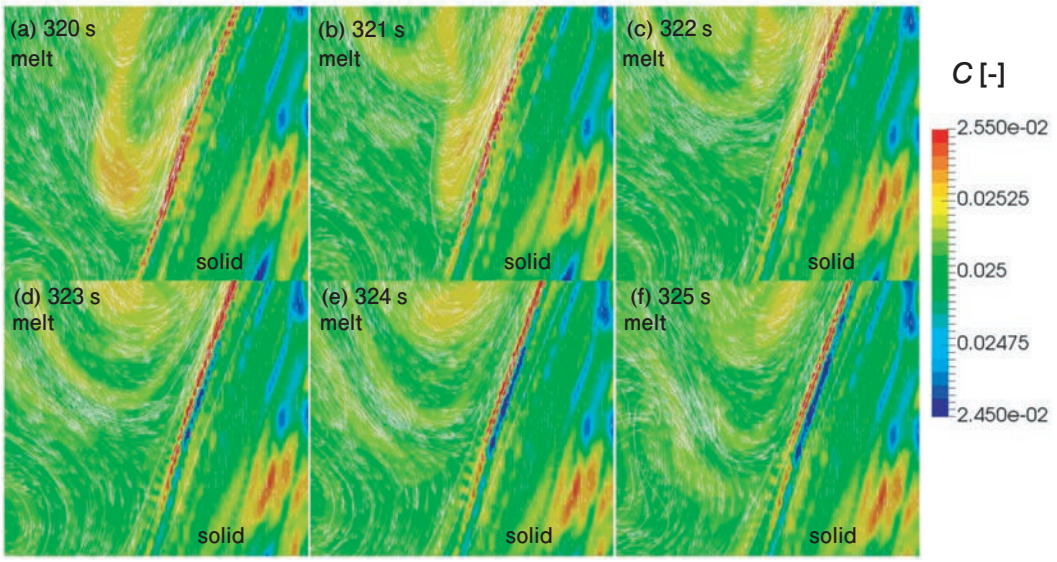

Fig. 14 Interaction between the slurry flow and stripped-pattern channel-type segregations in a large billet at a casting speed of 100 mm/min in the location where the upward buoyant flow is developed along the solidification front. The simulated time is (a) 320, (b) 321, (c) 322, (d) 323,(e) 324, and (f) 325 s (Color figure online).

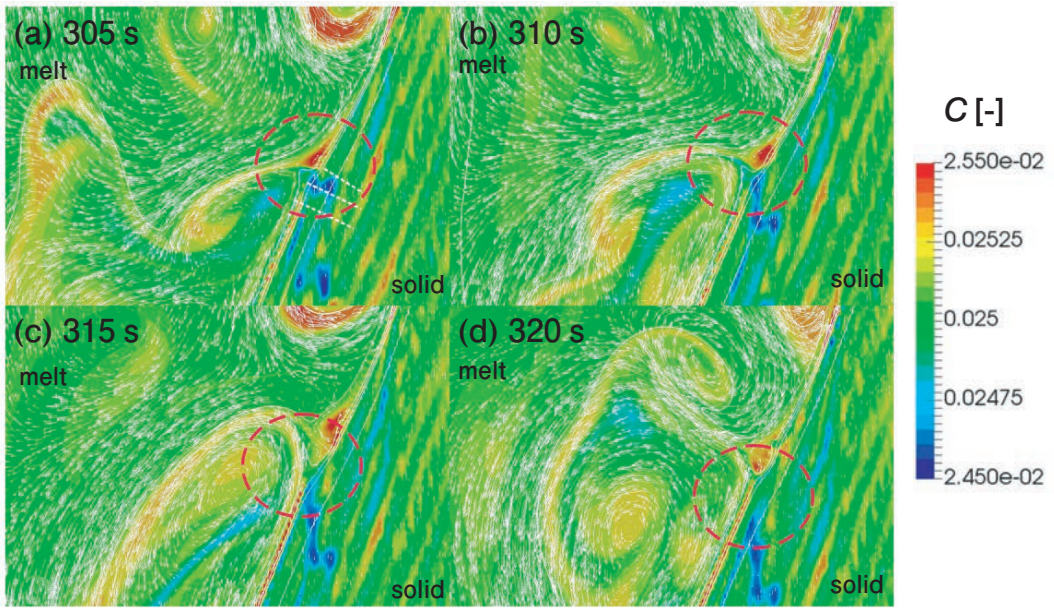

Fig. 15 Interaction between the slurry flow and vertically aligned negative channel-type segregations in a large billet at the casting speed of 100 mm/min in the flow separation zone. The simulated time is (a) 305, (b) 310, (c) 315, and (d) 320 s (Color figure online).

casting. As seen from Fig. 12, the channel-type segregations are formed when the casting speed is slow. It suggests that the channel-type segregations unlikely to be formed due to the downward flow, which is caused by motion of ingot in a DC casting.

4. Conclusion

In the present study, we investigated the generation mechanism of channel-type macro-segregations in a DC casting by numerical simulation. Particularly, the effects of volume shrinkage flow due to the phase transition and slurry flow on the macro-segregations were investigated. The channel-type macro-segregations and their formation mechanism were predicted in the DC casting process for the first time. The results obtained in the present study can be summarized as follows:

1. The volume shrinkage flow causes formation of zones with high Mg concentration at the bottom part of ingot.
2. Besides, the volume shrinkage flow causes

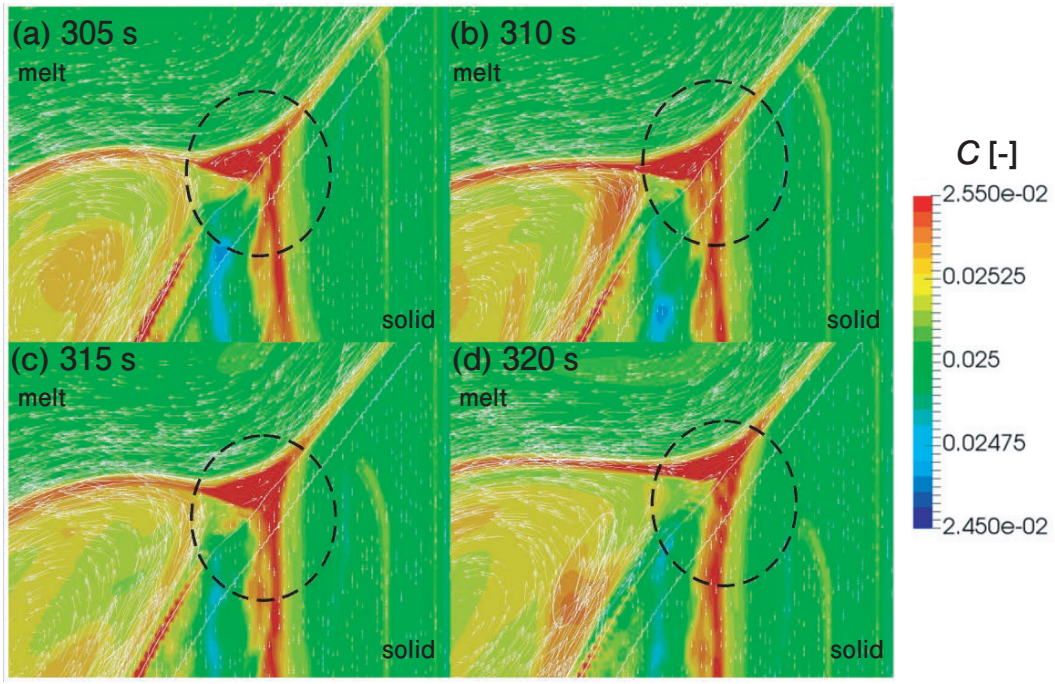

Fig. 16 Interaction between the slurry flow and Mg segregations in a billet with the radius of 200 mm at the casting speed of 100 mm/min inthe stagnant zone. The simulated time is (a) 305, (b) 310, (c) 315, and (d) 320 s (Color figure online).

formation of negative segregations along the center axis of billet, and this phenomenon is especially pronounced in the case of high casting speeds.

3. The slurry flow causes formation of the channel-type macro-segregations in the case of lower casting speeds and large billets.
4. The solutal buoyancy flow is the main cause of channel-type macro-segregations. Their formation condition can be evaluated by the solutal Rayleigh number.
5. The channel-type segregations can be easily formed in mold and directional casting while in the case of DC casting their formation becomes difficult because the
6. melt downward flow, generated by the downward motion of billet, prevents the development of upward solutal buoyancy flow.
7. The channel-type segregations are formed according the three mechanisms depending on the formation location.
8. The striped-pattern channel-type segregations are formed at the zone where an upward buoyancy flow is generated along the solidification front.
9. The high concentration zone caused by the solutal buoyancy flow delays the solidification, and creates a flow from the low concentration area toward the high concentration zone. Finally, channel-type segregations with stripped pattern are formed.
10. At the flow separation zones, the vertically aligned channel-type negative segregations are formed because the flow separation decreases the Mg concentration in the mushy zone.

REFERENCES

1) E.F. Emley: Int. Met. Rev., **21** (1976), 75–115.
2) R. Nadella, D.G. Eskin, Q. Du, and L. Katgerman: Prog. Mater. Sci., **53** (2008), 421–80.
3) D.G. Eskin, J. Zuidema, V.I. Savran, and L. Katgerman: Mater. Sci. Eng. A, **384** (2004), 232–44.
4) D.G. Eskin, V.I. Savran, and L. Katgerman: Metall. Mater. Trans. B, **36A** (2005), 1965–76.
5) D.G. Eskin, R. Nadella, and L. Katgerman: Acta Mater., **56** (2008), 1358–65.
6) W.D. Bennon and F.P. Incropera: Int. J. Heat Mass Transf., **30** (1987), 2161–70.
7) J. Ni and C. Beckermann: Metall. Trans. B, **22B** (1991), 349–61. https://doi.org/10.1007/BF02651234.
8) A.V. Reddy and C. Beckermann: Metall. Mater. Trans. B, **28B** (1997), 479–89.
9) H. Thevik, A. Mo, and T. Rusten: Metall. Mater. Trans. B, **30B** (1999), 135–42.
10) C.J. Vreeman, MJM. Krane, and F.P. Incropera: Int. J. Heat Mass Transf., **43** (2000), 677–86.
11) C.J. Vreeman and F.P. Incropera: Int. J. Heat Mass Transf., **43** (2000), 687–704.
12) C.J. Vreeman, J.D. Schloz, and MJM. Krane: J. Heat Transf.,

124 (2002), 947–53.
13) M. Zaloznik, B. Sarler, and D. Gobin: Mater. Technol., **38** (2004), 249–55.
14) M. Zaloznik and B. Sarler: Mater. Sci. Eng. A, **413–414** (2005), 85–91.
15) M. Zaloznik, S. Xin, and B. Sarler: Int. J. Numer. Methods, **18** (2008), 308–24.
16) M. Zaloznik, A. Kumar, H. Combeau, M. Bedel, P. Jarry, and E. Waz: Adv. Eng. Mater., **13** (2011), 570–80.
17) BCH. Venneker and L. Katgerman: J. Light Met., **2** (2002), 149–59.
18) D.G. Eskin, Q. Du, and L. Katgerman: Metall. Mater. Trans. A, **39A** (2008), 1206–12.
19) L. Heyvaert, M. Bedel, M. Založnik, and H. Combeau: Metall. Mater. Trans. A, **48A** (2017), 4713–34.
20) A. Pakanati, M. M'Hamdi, H. Combeau, and M. Zaloznik: Metall. Mater. Trans. A, **49A** (2018), 4710–21.
21) K.O. Tveito, A. Palanati, M. M'Hamdi, H. Combeau, and M. Zaloznik: Metall. Mater. Trans. A, **49A** (2018), 2778–94.
22) A. Pakanati, K.O. Tveito, M. M'hamdi, H. Combeau, and M. Zaloznik: Metall. Mater. Trans. B, **50B** (2019), 1773–86.
23) A. Pakanati, M. M'Hamdi, H. Combeau, and M. Zaloznik: IOP Cong. Ser. Mater. Sci. Eng., **861** (2020), 012040.
24) K. Fezi, A. Plotjiwski, and MJM. Krane: Numer. Hear Transf., **70** (2016), 939–63.
25) K. Fezi and MJM. Krane: Int. J. Cast Met. Res., **30** (2017), 191–200.
26) J. Coleman and MJM. Krane: Mater. Sci. Technol., **36** (2020), 393–402.
27) GSB. Lebon, G. Salloum-Abou-Jaoude, D. Eskin, I. Tzanakis, K. Pericleous, and P. Jarry: Ultrason. Sonochem., **54** (2019), 171–82.
28) GSB. Lebon, H.T. Li, J.B. Paterl, H. Assadi, and Z. Fan: Appl. Math. Model., **77** (2020), 1310–30.
29) H.T. Li, P. Zhao, R. Yang, J.B. Patel, X. Chen, and Z. Fan: Metall. Mater. Trans. B, **48B** (2017), 2481–92.
30) A. Noeppel, A. Ciobanas, X.D. Wang, K. Zaidat, N. Mangelinck, O. Bundenkova, A. Weiss, G. Zimmermann, and Y. Fautrelle: Metall. Mater. Trans. B, **41B** (2010), 193–208.
31) H. Combeau, M. Bellet, Y. Fautrelle, D. Gobin, E. Arquis, O. Budenkova, B. Dussoubs, Y.D. Terrail, A. Kumar, C.A. Gandin, B. Goyeau, S. Mosbah, T. Quatravaux, M. Rady, and M. Zaloznik: IOP Conf. Ser. Mater. Sci. Eng., **33** (2012), 012086.
32) A. Plotkowski and MJM. Krane: Comput. Mater. Sci., **124** (2016), 238–48.
33) F. Rösler and D. Brüggemann: Heat Mass Trans., **47** (2011), 1027–33.
34) C. Prakash and V. Voller: Numer. Heat Transf., **15** (1989), 171–89.
35) T. Yamamoto, H. Mirsandi, X. Jin, Y. Takagi, Y. Okano, Y. Inatomi, Y. Hayakawa, and S. Dost: Numer. Heat Transf. B, **70** (2016), 441–58.
36) T. Yamamoto and S.V. Komarov: J. Mater. Process. Technol., **294** (2021), art. no. 117116
37) D.C. Weckman and P. Niessen: Metall. Mater. Trans. B, **13B** (1982), 593–602.
38) S. Komarov and T. Yamamoto: Materials, **12** (2019), 3532.
39) Y. Du, Y.A. Chang, B. Huang, W. Gong, Z. Jin, H. Xu, Z. Yuan, Y. Liu, Y. He, and F.Y. Xie: Mater. Sci. Eng. A, **363** (2003), 140–51.
40) M. Leitner, T. Leitner, A. Schmon, K. Aziz, and G. Pottlacher: Metall. Mater. Trans. A, **48A** (2017), 3036–45.
41) R.I. Issa: J. Comput. Phys., **62** (1986), 40–65.
42) M. Bellet, H. Combeau, Y. Fautrelle, D. Gobin, M. Rady, E. Arquis, O. Budenkova, Y. Duterrail, A. Kumar, C.A. Gandin, B. Goyeau, S. Mosbah, and M. Zaloznik: Int. J. Therm. Sci., **48** (2009), 2013–16.
43) N. Mori and K. Ogi: Metall. Trans. A, **22A** (1991), 1663–72. https://doi.org/10.1007/BF02667378.

Takuya Yamamoto
Department of Chemical Engineering,
Osaka Metropolitan University,
Associate Professor,
Ph.D. (Eng.)

Keisuke Kamiya
Research Department Ⅱ,
Research & Development Center,
Marketing & Technology Division,
UACJ Corporation

Shohei Yomogida
Research Department Ⅱ,
Research & Development Center,
Marketing & Technology Division,
UACJ Corporation

Takashi Kubo
Research Department Ⅱ,
Research & Development Center,
Marketing & Technology Division,
UACJ Corporation,
Ph. D. (Eng.)

Masanori Tsunekawa
Research Department Ⅱ,
Research & Development Center,
Marketing & Technology Division,
UACJ Corporation

Keita Fukawa
Casting Technology Department,
Nagoya Works,
Flat Rolled Products Division,
UACJ Corporation

Sergey V. Komarov
New Industry Creation Hatchery Center,
Tohoku University, Project Professor,
Ph.D. (Eng.)